

Review

# *Pyplis*—A Python Software Toolbox for the Analysis of SO<sub>2</sub> Camera Images for Emission Rate Retrievals from Point Sources

Jonas Gliß<sup>1,2,3,\*</sup>, Kerstin Stebel<sup>1</sup>, Arve Kylling<sup>1</sup>, Anna Solvejg Dinger<sup>1,4</sup> , Holger Sihler<sup>5</sup> and Aasmund Sudbø<sup>3</sup>

<sup>1</sup> NILU—Norwegian Institute for Air Research, NO-2007 Kjeller, Norway; Kerstin.Stebel@nilu.no (K.S.); Arve.Kylling@nilu.no (A.K.); anna.solvejg.dinger@nilu.no (A.S.D.)

<sup>2</sup> Department of Physics, University of Oslo (UiO), NO-0371 Oslo, Norway

<sup>3</sup> Department of Technology Systems, University of Oslo (UiO), NO-2007 Kjeller, Norway; aasmund.sudbo@its.uio.no

<sup>4</sup> Institute of Environmental Physics (IUP), University of Heidelberg, D-69120 Heidelberg, Germany

<sup>5</sup> Max Planck Institute for Chemistry (MPIC), D-55128 Mainz, Germany; holger.sihler@mpic.de

\* Correspondence: jg@nilu.no; Tel.: +47-94885617

Received: 11 October 2017; Accepted: 11 December 2017; Published: 15 December 2017

**Abstract:** Ultraviolet (UV) SO<sub>2</sub> cameras have become a common tool to measure and monitor SO<sub>2</sub> emission rates, mostly from volcanoes but also from anthropogenic sources (e.g., power plants or ships). Over the past decade, the analysis of UV SO<sub>2</sub> camera data has seen many improvements. As a result, for many of the required analysis steps, several alternatives exist today (e.g., cell vs. DOAS based camera calibration; optical flow vs. cross-correlation based gas-velocity retrieval). This inspired the development of *Pyplis* (*Python plume imaging software*), an open-source software toolbox written in Python 2.7, which unifies the most prevalent methods from literature within a single, cross-platform analysis framework. *Pyplis* comprises a vast collection of algorithms relevant for the analysis of UV SO<sub>2</sub> camera data. These include several routines to retrieve plume background radiances as well as routines for cell and DOAS based camera calibration. The latter includes two independent methods to identify the DOAS field-of-view (FOV) within the camera images (based on (1) Pearson correlation and (2) IFR inversion method). Plume velocities can be retrieved using an optical flow algorithm as well as signal cross-correlation. Furthermore, *Pyplis* includes a routine to perform a first order correction of the signal dilution effect (also referred to as light dilution). All required geometrical calculations are performed within a 3D model environment allowing for distance retrievals to plume and local terrain features on a pixel basis. SO<sub>2</sub> emission rates can be retrieved simultaneously for an arbitrary number of plume intersections. Hence, *Pyplis* provides a state-of-the-art framework for more efficient and flexible analyses of UV SO<sub>2</sub> camera data and, therefore, marks an important step forward towards more transparency, reliability and inter-comparability of the results. *Pyplis* has been extensively and successfully tested using data from several field campaigns. Here, the main features are introduced using a dataset obtained at Mt. Etna, Italy on 16 September 2015.

**Keywords:** volcanic gases; SO<sub>2</sub>; remote sensing; UV cameras; image processing; analysis software; Python 2.7

---

## 1. Introduction

Sulfur dioxide (SO<sub>2</sub>) is a toxic gas emitted by anthropogenic and natural sources (e.g., power plants, ships, volcanoes). The pollutant has impacts on the atmosphere both on local and global

scales (e.g., particle formation, radiation budget, e.g., [1,2]). Furthermore, the monitoring of SO<sub>2</sub> emissions from active volcanoes can provide insight into the magmatic degassing behaviour and hence plays an important role for the development of new risk assessment approaches (e.g., [3–6], and references therein).

The gas composition of the emission plumes can, for instance, be studied using ground-based passive remote sensing techniques. The column-densities (CDs) of the gases in the plumes are quantified based on the absorption signature carried by scattered sunlight that has penetrated the plume. SO<sub>2</sub>-CDs, for instance, can be retrieved at ultraviolet (UV) wavelengths (i.e., around 310 nm) where it exhibits distinct absorption bands. Prominent examples for passive remote sensing instrumentation are the correlation spectrometer (COSPEC, [7]), or instruments based on the technique of Differential Optical Absorption Spectroscopy (DOAS, [8], e.g., [9,10]). Over the past decade, the comparatively young technique of UV SO<sub>2</sub> cameras has gained in importance, since it enables the study of volcanic SO<sub>2</sub> emissions at unprecedented spatial and temporal resolution (e.g., [11–15]). This is particularly helpful to study multiple sources independently (e.g., [16]) or to investigate volcanic degassing characteristics by studying periodicities in the SO<sub>2</sub> emission rates (e.g., [17–19] and references therein). The technique of UV SO<sub>2</sub> cameras has seen remarkable improvements over the past decade (e.g., [20–24]) and can now be considered one of the standard methods for ground-based remote sensing of SO<sub>2</sub> plumes. A drawback, however, is the low spectral resolution, restricting the technique to a single species and furthermore requiring external calibration.

The retrieval of SO<sub>2</sub> emission rates from plume imagery comprises several analysis steps that are summarised in Table 1 and are illustrated in the flowchart shown in Appendix Figure A1. Thanks to ongoing developments, today, researchers can choose between several methods for nearly all of the required steps (e.g., cell vs. DOAS calibration, velocity retrieval using optical flow vs. cross-correlation method).

Available software solutions include Vulcamera [25], the IDL<sup>®</sup> source code provided by [22] and Plumetrack [26]. The first two programs include routines for cell calibration and cross-correlation based plume velocity retrievals. The IDL<sup>®</sup> program also includes a routine to perform a first order correction for the signal dilution effect (commonly referred to as light dilution, e.g., [22]). The software Plumetrack provides an interface to calculate gas velocities using an optical flow algorithm and can be applied to pre-calibrated SO<sub>2</sub>-CD images in order to retrieve SO<sub>2</sub> emission rates.

**Table 1.** Analysis blocks for emission rate retrievals (for details see Section 2).

Analysis Block	Quantities	Analysis Options	Section
Geometrical Calculations	$\Delta s$		3.1
Plume Background Analysis	$\tau_{\text{on}}, \tau_{\text{off}}, \tau_{\text{AA}}$		3.3
Camera Calibration	$S_{\text{SO}_2}$	Cell, DOAS	3.4
Plume Velocity Retrieval	$\langle \vec{v} \cdot \hat{n} \rangle$	Optical flow, cross-correlation	3.5
Emission rate	$\Phi_{\text{SO}_2}$	Signal dilution correction	3.6, 3.7

*Pyplis* ([27,28]) is a cross-platform, open-source software toolbox for the analysis of UV SO<sub>2</sub> camera data. The code is written in Python 2.7 and emerged from the idea of a common software platform incorporating the most relevant analysis methods, including recent developments. The most important features of *Pyplis* 1.0.0 are (details follow in Section 3):

1. 3D distance retrievals to plume and local terrain features at pixel-level,
2. several methods to retrieve plume background radiances,
3. cell and DOAS based camera calibration including two independent DOAS FOV search routines,
4. cross-correlation and optical flow based plume velocity retrievals,
5. histogram based correction for ill-posed optical flow vectors in low-contrast image regions,
6. image based correction for the signal dilution effect,

7. automated emission rate retrievals along linear plume intersections.

*Pyplis* comes with numerous example scripts providing an easy and comprehensive introduction into the software. The following Section 2 introduces the technique of UV SO<sub>2</sub> cameras and the required analysis steps for SO<sub>2</sub> emission rate retrievals. The implementation of the individual analysis methods is discussed in Section 3.

**2. Methodology**

2.1. UV SO<sub>2</sub> Cameras

UV SO<sub>2</sub> cameras analyse scattered sunlight that has penetrated a plume containing SO<sub>2</sub> gas. Plume optical densities (ODs)  $\tau$  are retrieved in two wavelength windows of approximately 10 nm width, using optical bandpass filters. One filter is centred around 310–315 nm, where SO<sub>2</sub> has strong absorption bands (referred to as SO<sub>2</sub> on-band). A second filter is situated around 330 nm, where SO<sub>2</sub> absorption is weak (SO<sub>2</sub> off-band). The latter is used to correct for additional broadband light extinction, for instance, resulting from aerosols or water droplets in the plume. From the retrieved ODs in both channels, the apparent absorbance (AA) of SO<sub>2</sub> ( $\tau_{AA}$ , e.g., [20]) can be retrieved as

$$\tau_{AA} = \tau_{on} - \tau_{off} = \ln \left( \frac{I_0}{I} \right)_{on} - \ln \left( \frac{I_0}{I} \right)_{off}, \tag{1}$$

where  $I$  and  $I_0$  denote the plume and plume background radiances, respectively, in both channels (on, off). Note that the method requires all additional optical densities in the on and off-band regime to be of broadband nature.

2.2. Image Analysis—Retrieval of  $S_{SO_2}$  Images

AA images are determined from a set of pre-processed (e.g., dark / offset corrected) plume and background images using Equation (1). Next, the AA images are converted into SO<sub>2</sub> column-density (CD) images, where

$$S_{SO_2}(i, j) = \int_{C_{ij}} c(x, y, z) ds \tag{2}$$

denotes the SO<sub>2</sub>-CD in the viewing direction  $C_{ij}$  of the image pixel  $i, j$ .  $c(x, y, z)$  is the concentration distribution of SO<sub>2</sub> in real world coordinates  $x, y, z$  (cf. Figure 1a) and  $ds = \sqrt{dx^2 + dy^2 + dz^2}$  is the integration differential.

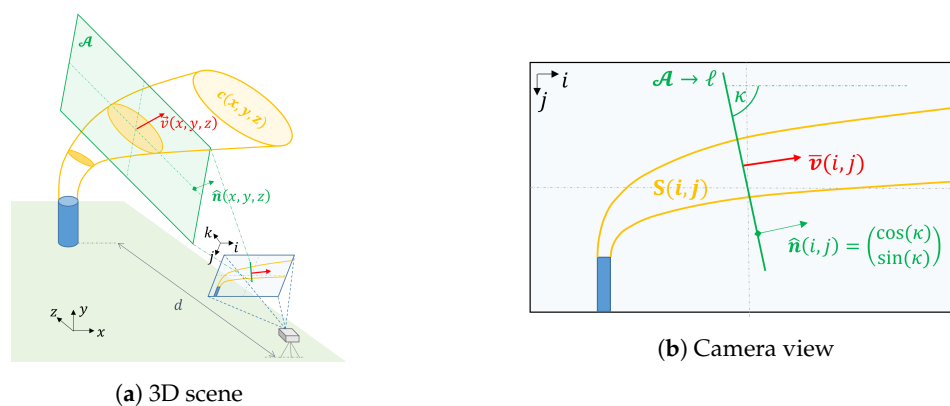


**Figure 1.** Measurement geometry—sketched (a) in three dimensions and (b) as the camera sees it. The emission plume is indicated in yellow colours, gas velocities in red. The orientation of the plume cross-section (PCS)  $\mathcal{A}$  (green colours) is aligned with the camera optical axis  $k$ .

The camera calibration (i.e., the conversion of AA values into SO<sub>2</sub>-CDs) can be performed either using gas cells (e.g., [11]) or a co-located DOAS spectrometer (e.g., [21]). The latter is more accurate in case aerosols are present in the plume [21,29]. The position and shape of the DOAS FOV within the camera images are required in order to perform the DOAS calibration. The DOAS FOV can either be measured experimentally (e.g., in the lab) or can be retrieved directly from the field data [21,30].

The camera calibration curve depends on the pixel-position in the images (e.g., [21]). This is due to shifts in the filter transmission curves for non-perpendicular illumination (i.e., off-axis image pixels), resulting in an increased SO<sub>2</sub> sensitivity towards the image edges (e.g., [31]). A first order correction for this effect can be performed using a normalised sensitivity correction mask retrieved from cell calibration data, as described in [21]. The impact of this effect can be dramatically reduced by placing the transmission filters between lens and detector rather than in front of the lens [31]. Please note that this effect of an increased SO<sub>2</sub> sensitivity towards the image edges is not to be confused with lens-vignetting effects, as discussed by [31].

### 2.3. Emission Rate Retrieval

SO<sub>2</sub> emission rates  $\Phi$  are retrieved from SO<sub>2</sub>-CD images by performing a discrete path integration along a suitable plume cross section (PCS) projected into the image plane, for instance a straight line  $\ell$  (illustrated in Figure 1b). Then,

$$\Phi(\ell) = f^{-1} \sum_{m=1}^M S_{\text{SO}_2}(m) \cdot \langle \bar{v}(m) \cdot \hat{n}(m) \rangle \cdot d_{\text{pl}}(m) \cdot \Delta s(m) \quad (3)$$

corresponds to the SO<sub>2</sub> emission rate through  $\ell$ , where  $m$  denotes one of a total of  $M$  sample positions along  $\ell$  in the image plane and  $\Delta s$  is the integration step length, measured in physical distances on the detector.  $f$  is the focal length of the camera,  $d_{\text{pl}}$  is the distance between camera and plume and  $\hat{n}$  is the normal of  $\ell$ .  $\bar{v}$  is a 2-vector containing projected plume velocities averaged in the viewing direction.

The plume distances  $d_{\text{pl}}$  can be estimated from the measurement geometry and require information about the camera position and viewing direction as well as the source position and the meteorological wind direction. The gas velocities are usually retrieved from the images directly either using cross-correlation based methods (e.g., [32]) or optical flow algorithms (e.g., [23]).

Equation (3) is equivalent to commonly used retrieval methods (e.g., [11,29]) and is based on the assumption that over or underestimations of the measured quantities  $S_{\text{SO}_2}$  and  $\bar{v}$  (e.g., due to non-perpendicular plume transects) cancel out in the emission rate retrieval. This is a valid approximation for typical measurement conditions (i.e., plume nearly perpendicular to the optical axis, and plume extent small compared to plume distance). However, care has to be taken for unfavourable geometries (e.g., tilted or overhead plume; retrieval close to the image edges), which may require additional corrections (e.g., [33]). The software Plumetrack [26] includes an alternative “2D” method to compute the emission rates, which considers all image pixels that are crossing the PCS line between consecutive frames. This method is not included in the current version of *Pyplis* but may be a valuable extension in a future release of the software.

If a locally uniform gas velocity can be assumed (i.e.,  $\bar{v}(i, j) \rightarrow \bar{v}$ ) and a planar PCS is used for the retrieval (i.e.,  $\hat{n}(i, j) \rightarrow \hat{n}$ ), then, Equation (3) can be further approximated as  $\Phi(\ell) \approx \langle \bar{v} \cdot \hat{n} \rangle \cdot \chi(\ell)$ , where

$$\chi(\ell) = f^{-1} \sum_{m=1}^M S_{\text{SO}_2}(m) \cdot d_{\text{pl}}(m) \cdot \Delta s(m) \quad (4)$$

denotes the integrated column amount (ICA) along  $\ell$ .



### 3.1. Geometrical Calculations

Geometrical calculations are performed within an instance of the `MeasGeometry` class (part of the `geometry.py` module). The plume distances  $d_{pl}$  (cf. Equation (3)) can be retrieved per pixel-column  $i$  using intersections of the respective viewing azimuth with the plume azimuth (see Figure 3). This requires specification of the camera position, viewing direction and optics (e.g., detector specifications, focal length), source coordinates and meteorological wind direction. The distances are determined based on the horizontal plume distance and the altitude difference between source and camera (i.e., assuming a horizontally aligned plume). It is pointed out that this approach may be inapplicable for complicated measurement geometries (e.g., overhead plumes), which would require a more detailed knowledge of the plume shape and altitude.

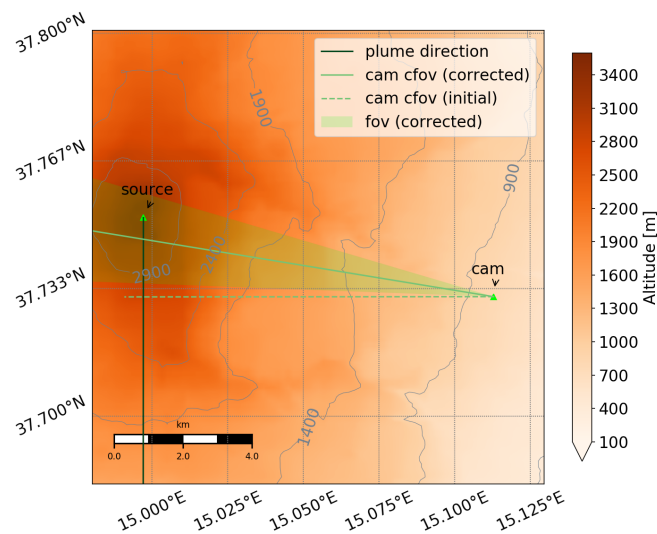


**Figure 3.** Measurement geometry 2D overview map of the measurement setup at Mt. Etna from the *Pyplis* example data. The map includes plume orientation (dark green line), camera azimuth retrieved using a compass (dashed light green line), the corrected camera azimuth (light green line) and the corresponding FOV (semi-transparent green), retrieved automatically using the pixel-position  $i, j$  of the Etna south-east crater within the images and the corresponding coordinates of the crater (longitude, latitude, altitude). The map was generated using an instance of the `MeasGeometry` class (see Section 3.1).

Further features of the `MeasGeometry` class include a routine to retrieve the camera viewing direction based on the position of distinct objects in the images (e.g., summit of volcano, cf. Figure 3), or the calculation of distances to topographic features in the images (cf. Figure 10). The `MeasGeometry` class makes use of the Geonum library [37], which is briefly introduced in Appendix A, and which provides automatic online access to topographic data from the NASA shuttle radar topography mission (SRTM, [38]) and also supports the ETOPO1 dataset [39]. Furthermore, 2D and 3D topographic overview maps of the measurement setup can be created automatically (as shown in Figure 3, see also Figure 10c).

### 3.2. Image Representation and Pre-Processing Routines

Images are represented by the `Img` class (`image.py` module). The `Img` class includes reading routines for all image formats supported by the Python Imaging Library (PIL, e.g., png, tiff, jpeg, bmp) as well as the FITS format (Flexible Image Transport System). It further allows to store relevant meta information (e.g., exposure and acquisition time, focal length, f-number) and includes several basic processing methods (e.g., smoothing, cropping or resizing using a Gaussian pyramid approach). The image data itself is loaded and stored as a 2D-NumPy array within an `Img` object. Automatic dark and offset

correction can be performed as described in Appendix C. `Img` objects can be saved as FITS files at any stage of the analysis (e.g., dark corrected image,  $\tau_{AA}$  image, calibrated SO<sub>2</sub>-CD image).

### 3.3. Retrieval of Plume Background Radiances

The calculation of the OD images in both wavelength channels requires the retrieval of the sky-background intensities  $I_0$  behind the plume (cf. Equation (1)). The `plumebackground.py` module provides several alternatives to retrieve the background intensities, either from the plume images directly or using an additional sky reference image ( $I_0$ -image). For the latter, several methods are available to correct for offsets and non-uniformities in the sky-background between the plume and  $I_0$ -image. The corrections are based on suitable sky-reference-areas in the plume image (rectangles or profile-lines, cf. Table 2) and use polynomials of a suitable order (e.g., linear or quadratic) to model the  $I_0$ -image such that the corresponding OD image satisfies  $\tau = 0$  within the specified sky reference areas.

If no  $I_0$ -image is available, the plume background radiances can also be estimated from the plume images directly using a masked 2D polynomial surface fit. The required mask specifies clear-sky image pixels that are considered during the fit. The mask can either be provided by the user or can be retrieved automatically using the function `find_sky_background` of the `plumebackground.py` module.

The `PlumeBackgroundModel` class (part of `plumebackground.py`) provides high level access to eight default methods for the background retrieval (in the code denoted with `mode`). These different retrieval methods are summarised in Table 2. Figure 4 shows four example plume on-band OD images calculated using the background modelling methods 0, 1, 4 and 6 (cf. Table 2). It is not intended to give a recommendation for a “best” method here, as this strongly depends on the data (e.g., availability of suitable reference areas; acquisition time and relative viewing direction of  $I_0$ -image; solar position).

**Table 2.** Available plume background modelling methods of the `PlumeBackgroundModel` class (cf. names of sky reference areas in Figure 4).

Method	$I_0$ -img	Corrections		
		Scaling	Vertical	Horizontal
1	yes	Scaling in <code>scale_rect</code>	None	None
2	yes	See 1	Linear correction using <code>scale_rect</code> and <code>ygrad_rect</code>	None
3	yes	See 1	Curvature correction by fitting polynomial of $n$ -th order using sky reference pixels along <code>vertical</code> profile line (default: $n = 2$ , i.e., quadratic polynomial)	None
4	yes	See 1	Linear correction (see 2)	Linear correction using <code>scale_rect</code> and <code>xgrad_rect</code>
5	yes	See 1	Curvature correction (see 3)	Linear correction (see 4)
6	yes	See 1	Curvature correction (see 3)	Curvature correction by fitting polynomial of $n$ -th order using sky reference pixels along <code>horizontal</code> profile line (default: $n = 2$ , i.e., quadratic polynomial)
0	no	Masked 2D polynomial surface fit		
99	yes	None (use $I_0$ -img as is)		

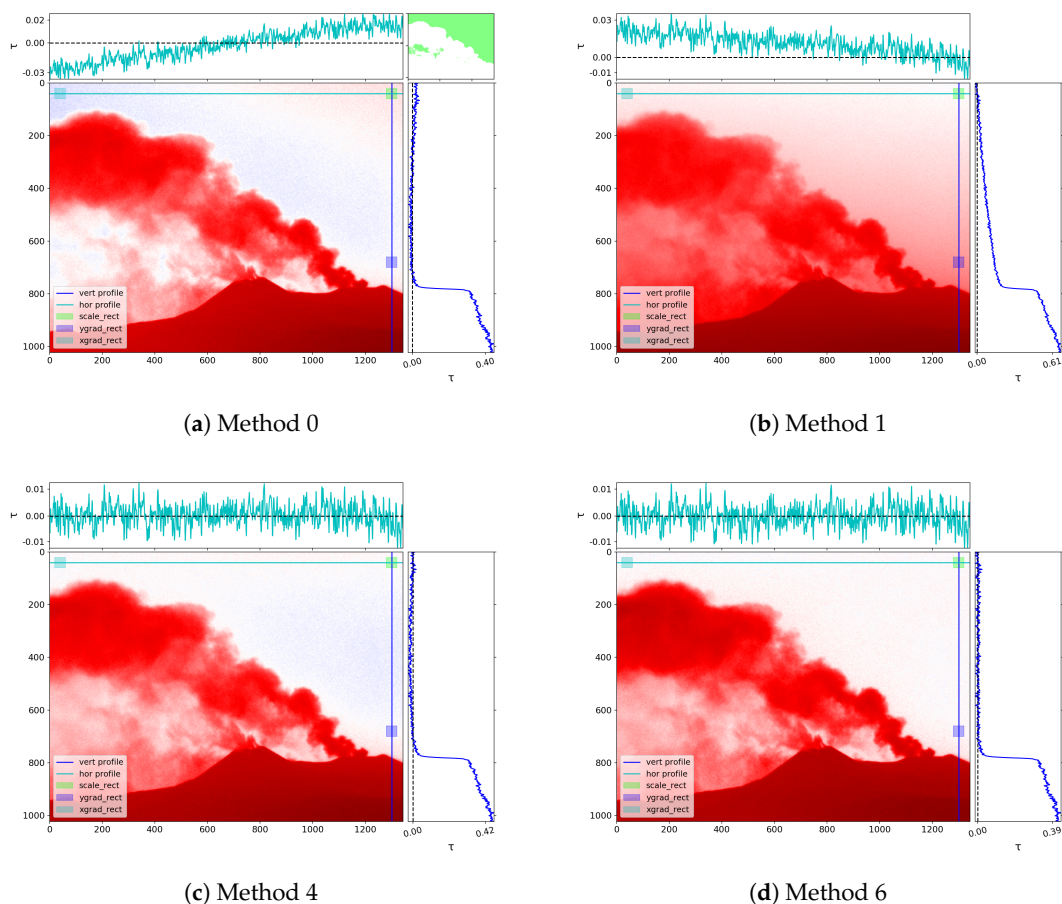


**Figure 4.** Plume background modelling. Four examples of on-band OD images ( $\tau_{on}$ ) determined using background modelling methods 0 (polynomial surface fit) and 1, 4 and 6 (based on  $I_0$ -image, cf. Table 2). Horizontal and vertical profiles are plotted on the top and on the right, respectively. The top-left plot (Method 0) further includes the mask specifying sky-reference pixels (green area) that was used for the polynomial surface fit. The plume and background images used for the displayed examples were recorded at 7:06 a.m. UTC and at 7:02 a.m. UTC, respectively.

### 3.4. Camera Calibration

The camera calibration can either be performed using data based on cuvettes (gas cells) filled with a known amount of  $\text{SO}_2$ -gas, or using plume  $\text{SO}_2$ -CDs retrieved from a co-located DOAS spectrometer (cf. Table 1).

#### 3.4.1. Calibration Using $\text{SO}_2$ Cells

Cell calibration can be performed using the `CellCalibEngine` class (`cellcalib.py` module) and requires a dataset containing both cell and sky background images. It is assumed that the camera is pointed into a gas and cloud free area of the sky and that the cells (containing different  $\text{SO}_2$ -CDs) are consecutively placed in front of the lens, such that they cover the whole FOV of the camera. Figure 5a shows a time-series of the image mean intensities retrieved from such a dataset. The individual cells can be identified by abrupt intensity drops in the time-series while the ambient background only changes gradually. The corresponding time-intervals for cell and background images can be specified by the user or, alternatively, detected automatically within an instance of the `CellCalibEngine` class (shown in Figure 5a, see also example scripts 0.7 and 5).

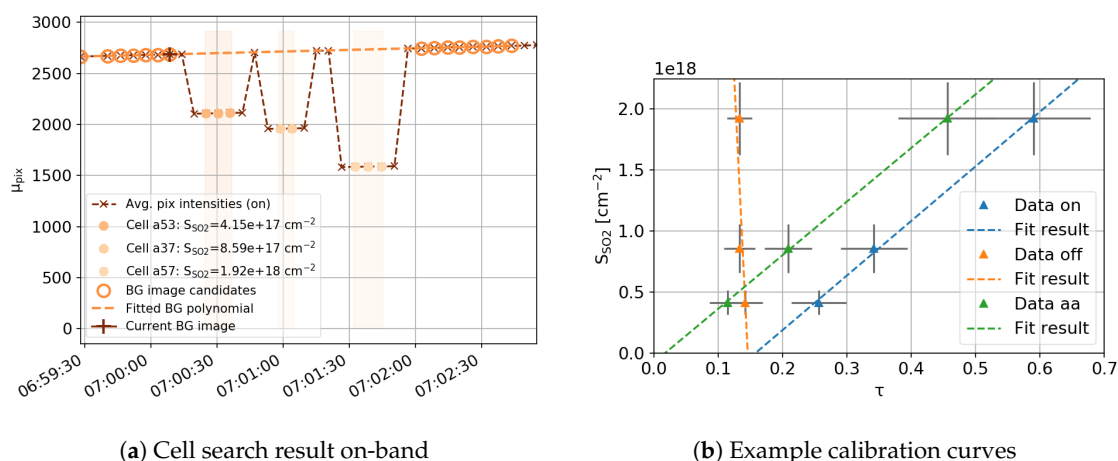


**Figure 5.** Cell calibration— (a) shows the output of the automatic cell search routine (included in the `CellCalibEngine` class); (b) shows example calibration curves for  $\tau_{\text{on}}$ ,  $\tau_{\text{off}}$  and  $\tau_{\text{AA}}$  images for the image center pixel from the dataset shown in (a). The error bars in (b) correspond to uncertainties in the cell  $\text{SO}_2$ -CDs from the DOAS analysis ( $y$ -axis errors) and the  $x$ -errorbars correspond to the min / max-range of the corresponding  $\tau$ -values over the entire image (arising from effects due to non-perpendicular illumination, see Section 2.2 for details).

Cell OD images in both channels ( $\tau_{\text{on}}$ ,  $\tau_{\text{off}}$ ) can be determined using a suitable background image. Care has to be taken for measurements performed at large solar zenith angles (early morning, late afternoon) due to rapid changes of the ambient sky intensity (cf. Figure 5a). In this case, the background image needs to be scaled to the sky intensity present at the acquisition time of each cell in order to calculate the OD images. This correction was performed for the data shown in Figure 5a (i.e., dashed line “Fitted BG polynomial”). It requires at least two background images, one recorded before, and a second one after the cells were put in front of the lens.

The calibration results (e.g., one AA image for each cell) are stored within `CellCalibData` objects together with the corresponding cell  $\text{SO}_2$ -CDs (which need to be provided by the user). Calibration curves can then be retrieved per image pixel or within a certain pixel neighbourhood. Figure 5b shows example calibration curves for  $\tau_{\text{on}}$ ,  $\tau_{\text{off}}$  and  $\tau_{\text{AA}}$  images.

### 3.4.2. Calibration Using DOAS Data

The DOAS calibration is performed using a set of plume optical density images (usually AA images) and a corresponding time-series of  $\text{SO}_2$ -CDs retrieved from a DOAS spectrometer. In a first step, the AA images are stacked into a 3D-NumPy array and merged in time with the DOAS data. The latter can be performed in three different ways (for details see Appendix D.1). The calibration data (i.e., merged time-series of  $\text{SO}_2$ -CDs and camera AA values within the DOAS FOV) can be retrieved by convolving the AA stack with a mask specifying position and shape of the DOAS field-of-view (FOV) within the image plane. The calibration data is stored within instances of the `DoasCalibData` class, which is also used to retrieve the calibration curve. The latter is done by fitting a polynomial of appropriate order to the calibration data. Optionally, the fit can be performed using a weighted regression, to account for statistical uncertainties in the DOAS  $\text{SO}_2$ -CDs (e.g., fit-errors, cf. Figure 6). `DoasCalibData` objects can be stored using the FITS standard (including the FOV mask).

Note that the DOAS calibration curve is only valid within the image pixel area covered by the DOAS FOV. This is due to cross-detector variations in the  $\text{SO}_2$  sensitivity (see Section 2.2) and can be corrected for using a mask retrieved from a cell calibration dataset. The mask is determined by fitting a 2D polynomial to a cell AA image (see prev. Section 3.4.1), which is then normalised to the centre-position of the DOAS FOV (illustrated in example script 7). Please also note that `Pyplis`

cannot perform the DOAS analysis. Thus, the SO<sub>2</sub>-CDs need to be retrieved using a suitable 3rd party software (e.g., DOASIS, [40]).

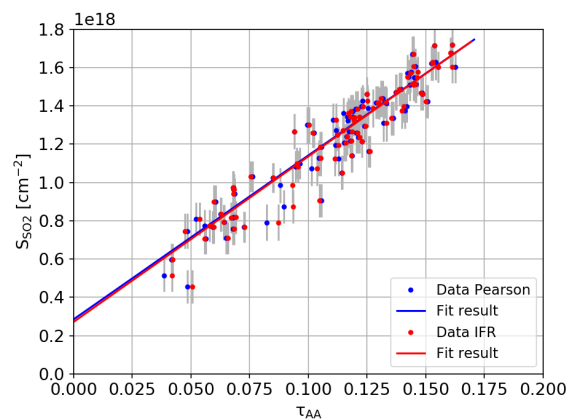


**Figure 6.** DOAS calibration curves. Plot showing example DOAS calibration data corresponding to the two different FOV parametrisations shown in Figure 7. The fit was performed using a first-order weighted polynomial fit. The weights were calculated using the relative errors  $\Delta S_{SO_2} / S_{SO_2}$  of the DOAS SO<sub>2</sub>-CDs. The  $y$ -axis offset is likely due to uncertainties in the DOAS retrieval (e.g., due to O<sub>3</sub> interference) and is compensated by the calibration.

### 3.4.3. DOAS FOV Search

*Pyplis* includes two routines to retrieve the DOAS FOV mask (included in the `DoasFOVEngine` class) based on a stack of AA images and a DOAS data vector:

1. Pearson routine: this method loops over all image pixels in the AA stack and determines the Pearson correlation coefficient between the corresponding AA time-series ( $\tau_{AA}(t)$ ) and the DOAS SO<sub>2</sub>-CD vector ( $S_{SO_2}(t)$ ). The method yields a correlation image as shown in Figure 7a, from which the pixel coordinate with highest correlation ( $i_0, j_0$ ) is extracted (see also [21]). Assuming a circular FOV shape, the pixel extent of the FOV is estimated around  $i_0, j_0$ , by iteratively searching the disk radius with highest correlation between the AA and the DOAS time-series.
2. In-operation field-of-view retrieval (IFR) routine: this method is based on [30] and uses an inversion algorithm to retrieve the FOV. Position and shape of the FOV is parametrised by fitting a 2D Super-Gaussian to the retrieved FOV distribution (shown in Figure 7b, see Appendix D.2 for details).

The retrieved FOV information (position, shape, convolution mask) is represented by the `DoasFOV` class and can be stored as a FITS file.

### 3.5. Plume Velocity Analysis

Plume velocities can be retrieved either using the ICA cross-correlation method or using an optical flow algorithm. Both methods yield displacement estimates in units of pixels / time. These are converted into plume gas velocities based on the measurement geometry (`MeasGeometry`, see Section 3.1). The relevant code is implemented in the `plumespeed.py` module.

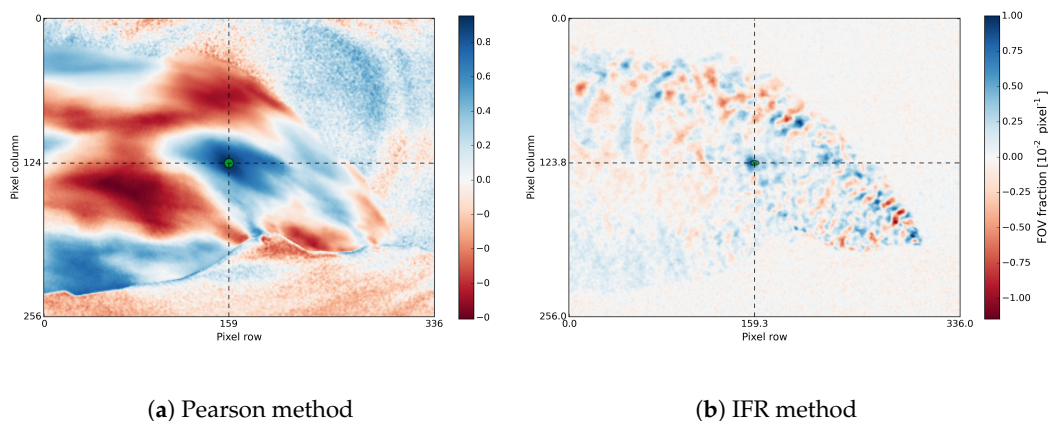


**Figure 7.** DOAS FOV search. DOAS FOV search results using (a), the *Pearson* and (b), the *IFR* method. The *Pearson* method (a) yields an FOV centered at  $i = 159, j = 124$  and a disk radius of four pixels. For the *IFR* retrieval (b), a tolerance factor of  $\lambda = 2 \times 10^{-3}$  was chosen and a Super-Gaussian (without tilt) was fitted to the correlation image yielding an FOV centered at  $i = 159.3, j = 123.8, \sigma = 7.1$ , asymmetry parameter  $a = 1.9$  and a shape parameter of  $b = 0.3$  (for details see Equation (A2)). The retrieved FOV positions show good agreement. Note that the FOV was retrieved from downsampled images (Gauss pyramid level 2).

### 3.5.1. Velocity Retrieval Using the ICA Cross-Correlation Method

For the cross-correlation method, ICA time-series (see Equation (4)) are determined using two PCS lines located at different positions downwind the emission source. Ideally, the PCS lines should be parallel and should cover an entire plume cross-section (indicated in Figure 8, left).

In a first step, the two time-series are re-sampled onto a regular grid (default is 1 s resolution). In a second step, a correlation analysis is applied to the re-sampled data vectors in order to find the time lag corresponding to the highest correlation between both signals. The method yields one average velocity vector, which is representative for the used image region and time-series. Note that the method intrinsically assumes that the average plume propagation direction  $\vec{\varphi}$  in the  $i, j$ -plane is aligned with the PCS normal (i.e.,  $\vec{\varphi} \parallel \hat{n}$ ) and furthermore that  $\text{SO}_2$  is conserved between the two PCS lines used. Figure 8 shows results from an example cross-correlation analysis, resulting in a plume velocity of 3.5 m/s.

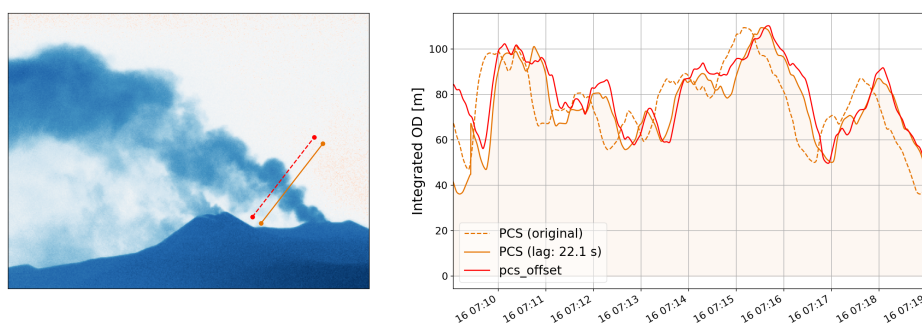


**Figure 8.** Plume velocity retrieval using the cross-correlation method applied to a time-series of on-band OD ( $\tau_{\text{On}}$ ) images. Left: example plume image including the two used PCS lines. Right: Time-series of the integrated optical densities along both lines (orange dashed and cyan line) in addition to the PCS signal shifted using the retrieved correlation lag of 22.1 s (orange profile). The analysis yields an average gas velocity of 3.5 m/s.

### 3.5.2. Optical Flow Based Velocity Retrievals

Optical flow velocity retrievals are performed using the Farneback algorithm [41], which is implemented in the OpenCV library [42]. The algorithm can estimate motion at the pixel-level by tracking local contrast features between consecutive frames. Note, however, that optical flow algorithms may fail to detect motion in extended homogeneous image areas. In this case, appropriate corrections may be required (e.g., [43]).

All relevant calculations for optical flow based velocity retrievals are performed within the `OptflowFarneback` class. The class includes the Farneback algorithm itself as well as several pre- and post-analysis routines. The latter includes a routine that can detect and correct for unphysical motion estimates in homogeneous image regions based on the method proposed by [43]. The correction identifies the local average velocity vector using peaks in histograms of an optical flow motion field.

The Farneback algorithm itself requires specification of several input parameters (see e.g., [23], or OpenCV documentation). The *Pyplis* default settings follow the suggestions of [23]. An example flow field is shown in Figure 9 including results from the histogram post analysis within a narrow region-of-interest (ROI) around an example retrieval line. The latter yields an average velocity magnitude of  $4.2 (\pm 0.4)$  m/s and a predominant movement direction of  $\varphi = -65 (\pm 14)^\circ$  within the image plane. Optical flow plume velocity retrievals, including the histogram post analysis method, are introduced in example script 9 (see Table A2).

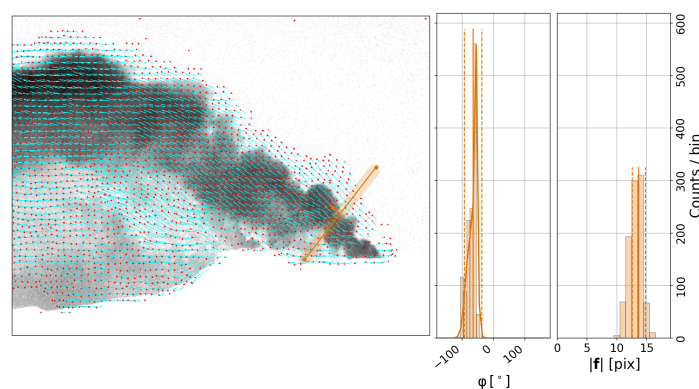


**Figure 9.** Plume velocity optical flow. Left: example optical flow vector field (blue lines with red dots depicting the movement direction) calculated using the Farneback algorithm. Middle, right: histograms of the flow vector orientation angles  $\varphi$  and magnitudes  $|f|$ , respectively, corresponding to the ROI shown in the left image (semi-transparent rectangular area around the displayed PCS line). From the latter, a plume velocity of  $4.2 (\pm 0.4)$  m/s and a predominant movement direction of  $\theta = -65 (\pm 14)^\circ$  was retrieved using first and second moments of the displayed histogram distributions.

### 3.6. Image Based Signal Dilution Correction

A correction for the signal dilution effect (see Section 2.4) can be performed using the `DilutionCorr` class. The method is based on [22] and uses the model function

$$I_{\text{meas}}(\lambda) = I_0(\lambda)e^{-\epsilon(\lambda)d} + I_A(\lambda)(1 - e^{-\epsilon(\lambda)d}) \quad (5)$$

to retrieve atmospheric extinction coefficients  $\epsilon$  in the on and off-band regime. Here,  $\lambda$  denotes the wavelength,  $I_{\text{meas}}$  are measured intensities of dark terrain features within the images,  $d$  is the distance to these features and  $I_0$  their initial intensity. The ambient intensity  $I_A$  can be approximated using gas free sky areas in the plume images [22]. For the retrieval, a set of measured intensities  $I_{\text{meas}}$  is extracted from vignetting corrected plume images using suitable terrain features (e.g., pixels along a volcanic flank). These intensities are fitted to Equation (5) (as a function of their distance  $d$ ) in order to retrieve the extinction coefficients in both wavelength regimes. The required distances  $d$  to the features

can be retrieved automatically, based on intersections of individual pixel viewing directions with the local topography (using the Geonum library; for details, see Appendix A).

The plume images can then be corrected for the signal dilution effect using the retrieved extinction coefficients (see Equation (4) in [22]). The correction is only applied to plume pixels (e.g., using a  $\tau_{AA}$  threshold mask). The required plume distances can be retrieved from the measurement geometry (for details, see Section 3.1).

Figure 10 shows results of an example dilution correction using an on and off-band image from the Etna example data, recorded at 6:45 a.m. UTC. Extinction coefficients of  $\epsilon_{\text{on}} = 0.0743 \text{ km}^{-1}$  (Figure 10a) and  $\epsilon_{\text{off}} = 0.0654 \text{ km}^{-1}$  (Figure 10b) were retrieved using the two topographic profile lines shown in Figure 10c,d. The correction yields an emission rate of  $4.8 (\pm 1.2) \text{ kg/s}$  using the PCS line shown in Figure 10d. The emission rate of the uncorrected image is  $1.6 (\pm 0.8) \text{ kg/s}$ , corresponding to an underestimation of approximately 67% at an average plume distance of  $10.4 (\pm 0.1) \text{ km}$ .

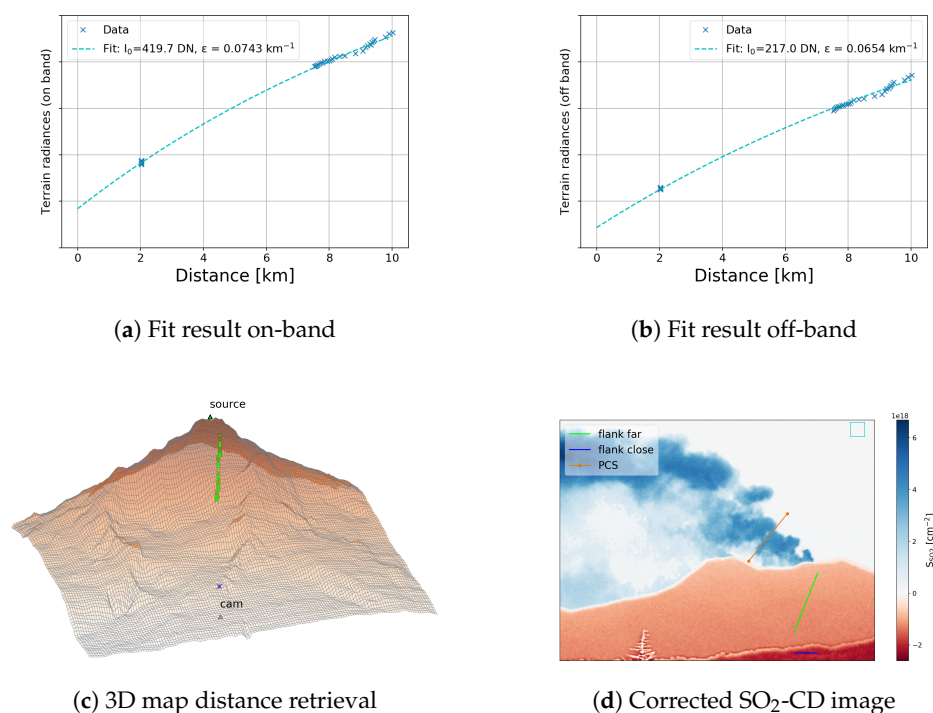


**Figure 10.** Signal dilution correction. (a) and (b) show the fit results of an example dilution analysis for the on and off-band regime, respectively; (c) shows a 3D map of the camera scene and (d) a dilution corrected  $\text{SO}_2$ -CD image. The terrain features used for the dilution analysis are indicated in (c) and (d) (blue and lime coloured lines); (d) further includes the image region used to estimate the ambient intensity  $I_A$  (blue rectangle) and an example PCS line used to compare emission rates before and after the correction.

### 3.7. Emission Rate Retrieval

Emission rates can be determined using the `EmissionRateAnalysis` class. The analysis is performed based on an image list containing calibrated  $\text{SO}_2$ -CD images (see also Appendix E.2) and a specification of one or more retrieval PCS lines (`LineOnImage` objects, cf. Figure 2). Plume velocities can be provided by the user (e.g., using the result of a cross-correlation analysis, see Section 3.5.1) or can be retrieved automatically during the emission rate analysis using the Farneback optical flow routine (see Section 3.5.2). For the latter, three options are available:

1. *flow\_raw* → the raw output of the Farneback algorithm is used. This should only be done if it can be assured that the algorithm yields reliable output in the considered plume area (i.e., ROI around the PCS line) and for all images of the time-series.
2. *flow\_histo* → performs the histogram post-analysis proposed by [43] (cf. Section 3.5.2). The retrieved local average velocity vector for each PCS line is then used as a velocity estimate for the corresponding retrieval line.
3. *flow\_hybrid* → reliable motion vectors from the flow field are used while unreliable ones are identified and replaced based on the histogram post-analysis (see previous point).

Figure 11 shows results from an emission rate analysis for the Etna test data (upper panel) including plume velocities retrieved using the *flow\_hybrid* method (lower panel). The AA images were calculated from dilution corrected on and off-band plume images using background modelling method 6 (cf. Section 3.3) and were corrected for cross-detector sensitivity variations using a mask retrieved from cell “a53” (cf. Figure 5a). The AA images were calibrated using the Pearson DOAS calibration curve shown in Figure 6.

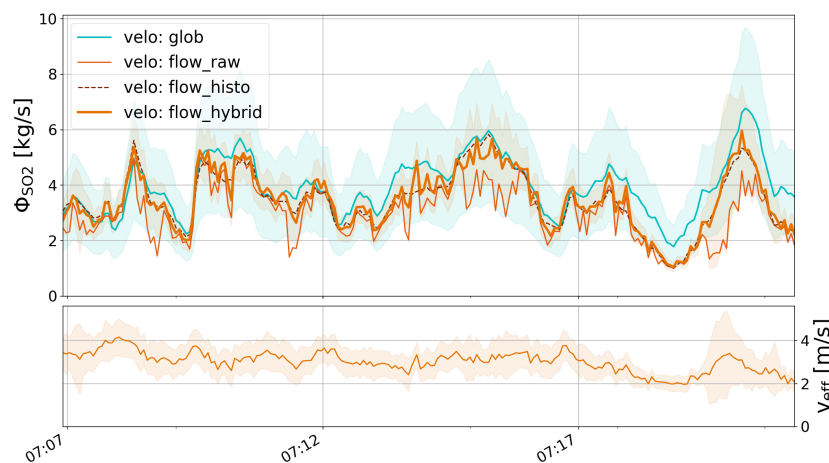


**Figure 11.** Emission rate retrieval. Emission rates (top) and plume velocities (bottom) of the Etna example dataset on 16 September 2015 between 7:06 a.m. and 7:22 a.m. UTC using the retrieval line “PCS” shown in Figure 8. The analysis was performed using (1) a global velocity of 3.5 m/s (cyan, from cross-correlation analysis); (2) the raw output of the Farneback algorithm (thin orange); (3) using the *flow\_histo* method (thin dashed brown) and (4) using the *flow\_hybrid* method (bold orange). The retrieved effective velocities are plotted in the lower panel and correspond to the average velocities along the PCS line using the *flow\_hybrid* method. Uncertainties are displayed as shaded areas.

#### Remark on Performance

The emission rate analysis (cf. Figure 11) was performed using a Gaussian pyramid level of 1 (i.e., reduction of image size by a factor of 2). For these settings, the typical computation time to calculate a calibrated SO<sub>2</sub>-CD image from the raw data amounts to approximately 0.2 s using an Intel(R) Core(TM) i7-6500U CPU (2.50 GHz, 8 GB RAM) (Santa Clara, CA, USA). Approximately the same time of 0.2 s is required to compute the optical flow between two frames at this pyramid level (cf. Appendix Table A1). For the discussed dataset of 209 on-band plume images, this results in a total computation time of about two minutes, including the four different velocity retrieval methods introduced above and shown in Figure 11. Note that the latter does not include the time to compute the DOAS FOV and calibration data, nor the time required for the cross-correlation velocity retrieval, since these analyses were performed beforehand (for details, see Appendix B and example script 12).

### 3.8. Remark on Uncertainties

The uncertainties in the emission rates (cf. shaded areas in Figure 11) were calculated using Gaussian error propagation (see method `det_emission_rate` of the `fluxcalc.py` module) considering (1) uncertainties in the meteorological wind direction and camera viewing direction (accessible using the method `plume_dist_err` of the `MeasGeometry` class); (2) uncertainties in the calibration curve (based on slope error retrieved from covariance matrix of fit result, accessible using the attribute `slope_err` of either the `DoasCalibData` or the `CellCalibData` class); and (3) the uncertainties in the velocity retrieval. For optical flow based velocity analyses, the uncertainties are calculated as discussed in Section 2.4.1 in [43], based on the retrieved effective velocities  $v_{\text{eff}} = \langle \bar{v} \cdot \hat{n} \rangle$  along  $\ell$  (cf. Equation (3)). Note that *Pyplis* does not provide a method to estimate the uncertainties of cross-correlation based velocity retrievals. These need to be provided by the user (cf. example script 12). The errors in the effective velocities can be accessed via the `velo_eff_err` attribute of the `EmissionRates` class. Note that all uncertainties computed by *Pyplis* are assumed to be of statistical nature. Hence, they do not account for any potential systematic errors, for instance arising from ill-constrained optical flow vectors when using the `flow_raw` retrieval method (see discussion in Section 2.4.1 in [43]).

## 4. Conclusions

In this paper, the software package *Pyplis* was introduced. *Pyplis* contains an extensive collection of relevant algorithms for the analysis of UV SO<sub>2</sub> camera data, particularly for the retrieval of emission rates from SO<sub>2</sub>-emitters (e.g., volcanoes, power plants, ships).

Apart from established analysis methods, such as cross-correlation based velocity retrievals (e.g., [32]) or cell and DOAS calibration (e.g., [21]), *Pyplis* incorporates more recent developments. These include an implementation of the DOAS FOV retrieval algorithm proposed by [30], a routine to correct for the signal dilution effect based on [22], or pixel based gas velocity retrievals using an optical flow algorithm (e.g., [23]). The latter incorporates a method to detect and correct for ill constrained optical flow motion-vectors based on [43]. Furthermore, *Pyplis* includes a framework to perform a detailed 3D-analysis of the observed camera scene including automatic online access to high resolution topography data from the SRTM dataset. This enables, for example, to retrieve the camera viewing direction based on distinct topographic features in the images (e.g., volcano summit), or to calculate distances between the camera and the local topography at a pixel-level. The latter is of particular relevance for the image based correction of the signal dilution effect.

Due to this extensive collection of algorithms, *Pyplis* provides flexibility with regard to the analysis strategy and is highly adaptable to different data situations. The object oriented architecture of the API gives intuitive access to the main features and makes it easy to compare individual methods (e.g., different plume velocity retrievals, as illustrated in this paper). *Pyplis* is open-source and can be operated both on Windows and Unix machines. Thus, it is well suited for inter-comparison studies, the exchange of analysis results or for the development and verification of new methods.

The *Pyplis* installation includes numerous example scripts that were used in this paper to introduce the main features of the software. The examples are based on a 15 min dataset recorded at Mt. Etna, Italy in September 2015, which is freely available and can be downloaded from the website.

Finally, the authors wish to point out that *Pyplis* may also be used for other applications based on the same measurement principle (e.g., NO<sub>2</sub> cameras) and that parts of it can also be useful for other remote sensing applications (e.g., the engine for geometrical calculations). The *Pyplis* software is hosted on GitHub ([27,28]). The code documentation and further information (e.g., installation instructions) can be found on the documentation website (see [27,28]).

**Acknowledgments:** The authors like to thank the *Atmosphere and Remote Sensing* group from the Institute of Environmental Physics in Heidelberg, Germany for providing image data for test purposes and for collaboration during the Etna field campaign in 2015. The work of K.S., A.K. and A.S.D. was supported by the European Research Council (ERC) under the European Union's Horizon 2020 research and innovation programme under grant agreement No 670462 (COMTESSA). J.G. wishes to thank Torbjørn Skauli, Matthias Vogt, and Axel Donath

for helpful discussions related to the development of the software and the drafting of the manuscript. Furthermore, the authors wish to thank the Editor Cecile Zheng for support during the review process and four anonymous referees for very helpful comments and suggestions.

**Author Contributions:** J.G. designed, developed and tested the software including the example scripts and wrote the manuscript. K.S., A.S.D., A.K., H.S. and A.S. contributed to the API design (selection of implemented methods/algorithms) and helped with testing and debugging the code. H.S. provided the IFR algorithm and wrote the corresponding part in the paper.

**Conflicts of Interest:** The authors declare no conflict of interest.

## Abbreviations

The following abbreviations are used in this manuscript:

UV	Ultraviolet
CD	Column density
DOAS	Differential optical absorption spectroscopy
FOV	Field of view
OD	Optical density
AA	SO <sub>2</sub> apparent absorbance
PCS	Plume cross section
ICA	Integrated column amount
API	Application programming interface
IFR	In-operation field-of-view retrieval

## Appendix A. The Geonum Python library

The *Pyplis* class `MeasGeometry` (see Section 3.1) makes use of the Python library Geonum [37]. Geonum was developed by Jonas Gliß in parallel to *Pyplis* and features vector based geographical calculations in three dimensions as well as access and handling of high resolution topographic data. It supports topographic data based on the Etopo1 global relief model [39] and from the NASA shuttle radar topography mission (SRTM, [38]). The latter can be accessed and downloaded automatically within Geonum from the SRTM online database (for details, see information on the Geonum [37] website).

### Appendix A.1. Pixel Based Retrieval of Distances to Local Terrain Features

Distances to topographic features can be retrieved at the pixel-level based on the camera position and viewing direction by calculating the intersections of individual pixel viewing directions (i.e., azimuth and elevation angle) with the local topography. This is particularly helpful for the image based correction of the signal dilution effect (see Section 3.6 and Figure 10).

## Appendix B. Performance of Typical Analysis Chain

The time required to perform a full emission rate analysis with *Pyplis* (cf. Section 3.7) depends on many factors, most importantly on the performance of the computer, but also largely on the chosen analysis settings and the methods used. Below, we provide information about the typical computation time required to calculate a calibrated SO<sub>2</sub>-CD image from the raw data and to compute the optical flow, using an Intel(R) Core(TM) i7-6500U CPU (2.50 GHz, 8 GB RAM) and the Envicam-2 image type (i.e., 12 bit, 1344 × 1024 pixels). The main analysis steps per image comprise:

1. Image import and dark and offset correction (on and off-band).
2. Further image preparation operations (e.g., noise reduction using Gaussian blurring filter, size reduction using Gaussian pyramid).
3. Plume background modelling (on, off) and calculation of  $\tau_{AA}$ -image.
4. Image calibration (i.e., requires availability of calibration curve).
5. Optional: computation of optical flow field.

Table A1 summarises typical computation times for these steps that are performed for each image during the emission rate analysis. Further settings for this performance analysis (e.g., background modelling method) correspond to the settings provided in Section 3.7. Note that here we omit the discussion of potential additional analysis procedures that may be required and that are typically performed prior to the emission rate analysis (e.g., dilution correction, DOAS and / or cell calibration, cross-correlation velocity retrieval, cf. Figure 2). These highly depend on the chosen settings and often include looping over a number of images and pre-computation of OD images (e.g., DOAS FOV search, cross-correlation velocity analysis) and we encourage the reader to use the corresponding example scripts for individualised performance tests of these additional analysis procedures.

**Table A1.** Performance analysis of the five image preparation steps listed above, dependent on Gaussian pyramid level (*pyrlevel*) and Gaussian blurring (*blur*) including the relative percentage impact of the optical flow computation.

Blur	Pyrlevel	Computation Time [s]		
		Image Preparation (Steps 1–4)	Optical Flow (Step 5)	Total
10	0	0.350	0.823 (70 %)	1.173
0	0	0.188	0.813 (81 %)	1.001
0	1	0.205	0.202 (50 %)	0.407
0	2	0.203	0.103 (34 %)	0.306

## Appendix C. Dark and Offset Correction

*Pyplis* includes two options to perform dark and offset corrections for image data. Both methods require access to the exposure time of the images (e.g., from the image file names, see also Appendix F).

### 1. Option 1: Modelling of Dark/Offset Image

The correction is performed based on two dark images, one being recorded at short(est) exposure time (offset signal  $O$ ) and the second one at long(est) exposure time (dark current + offset signal,  $D$ ). A dark image is then calculated based on the exposure time  $t_{\text{exp}}$  of the input image  $I$  using the following formula:

$$D_{\text{mod}} = O + \frac{(D - O) * t_{\text{exp},I}}{(t_{\text{exp},D} - t_{\text{exp},O})}. \quad (\text{A1})$$

This mode is, for instance, used for the Envicam-2 camera type (NILU, Norway, for details see [24]). The corresponding method `model_dark_image` is part of the *processing.py* module.

### 2. Option 2: Subtraction of Dark Image

Dark and offset correction is performed by subtracting a single dark image  $D$  (containing dark and offset), which, thus, needs to be recorded at the same camera exposure time. This mode is, for instance, used for the HD-Custom camera (Heidelberg, Germany, for details see [24]).

The detector dark current depends on the temperature. In case of temperature variations, it is therefore recommended to use dark images recorded close in time to a given plume image.

## Appendix D. Spectrometer FOV Search: Additional Information

### Appendix D.1. Temporal Merging of Image and DOAS Data

The `ImgStack` class includes three methods to merge a set of camera images (stacked within such an `ImgStack`) and a DOAS time series vector, both sampled on arbitrary irregular grids.

- **First Method: Averaging of Camera Images**

This method averages all images in the stack based on start/stop time stamps of the spectrometer data (i.e., the image sampling rate should be larger than the spectrum sampling rate). Spectra for which no image data could be found are removed.

- Second Method: Vice Versa Interpolation of Both Grids**  
 This method uses the unified sampling grid (all time stamps from both datasets) and performs interpolation of the DOAS data vector (at image acquisition time stamps) and vice versa. The method is slow compared to method 1 since each image pixel of the stack is interpolated. However, it results in more data points, which can be an advantage especially for short time series. This method can be significantly accelerated by reducing the image size or by only performing the analysis within a certain image region (c.f. example script no. 6, Table A2, script option: DO\_FINE\_SEARCH). The time series interpolation is done using the *pandas* Python library.
- Third Method: Nearest Data Point**  
 This method loops over all spectra and for each spectrum, finds the image which is nearest in time. This method is for instance used, if only the acquisition time stamps are provided and not the start / stop stamps of each exposure (which is required for the first method).

*Appendix D.2. FOV Determination Applying the IFR Method*

The In-operation Field of view Retrieval (IFR) method is an implementation of the method proposed by [30]. IFR applies a linear camera model to invert the FOV of a low-resolution instrument (in this case, a DOAS spectrometer) from imager data without a priori information (e.g., FOV position, size and shape). The inversion problem is typically under-determined for SO<sub>2</sub> camera applications. Therefore, the iterative LSMR method [44] is applied to retrieve the FOV coefficients depending on the regularisation parameter  $\lambda$ .

The choice of  $\lambda$  is somewhat arbitrary but may influence the IFR results depending on the input data quality. The default value is  $\lambda = 10^{-6}$ . However, in case only a small sample size is available,  $\lambda$  may need to be increased (e.g.,  $\lambda = 10^{-3}$ ) in order to produce meaningful results. A side effect of increasing  $\lambda$  is a spatial smoothing of the results potentially leading to unrealistic large FOVs. Figure 7b shows a sample FOV distribution retrieved from the Etna test data (88 images) using  $\lambda = 2 \times 10^{-3}$ .

In order to reach the final goal of gaining a calibration curve from the image stack containing AA images, individual images need to be convolved with the FOV of the low-resolution instrument. Therefore, a parametrised FOV is fitted to the IFR results, which is more applicable to ground-based instruments than the parametrisation proposed by [30]. We propose the following elliptical Super-Gaussian FOV parametrisation  $g$  of the IFR result depending on pixel coordinates  $i, j$  in horizontal and vertical direction, respectively:

$$g(i, j) = C + Ae^{-\left(\left[\frac{i-i_m}{\sigma}\right]^2 + \left[\frac{(j-j_m)a}{\sigma}\right]^2\right)^b}, \tag{A2}$$

where  $C$  is a constant offset,  $A$  the amplitude,  $i_m$  and  $j_m$  define the centre position,  $\sigma$  measures the width in  $i$ -direction, the asymmetry parameter  $a$  measures the ratio of the semi-axes (e.g.,  $a = 1$  yields a circular FOV), and  $b$  is the shape parameter of the Super Gaussian (e.g.,  $b = 1$  yields a Gaussian FOV,  $b = 10$  approximates a flat-disk FOV).

If an additional tilt of the FOV is required in case of an elliptical FOV, the above fit may be performed in a transformed coordinate system and

$$\begin{pmatrix} i' \\ j' \end{pmatrix} = \begin{pmatrix} \cos \theta & -\sin \theta \\ \sin \theta & \cos \theta \end{pmatrix} \begin{pmatrix} i - i_m \\ j - j_m \end{pmatrix} \tag{A3}$$

defines the transformation into tilted coordinates  $i'$  and  $j'$ . Equation (A2) is then replaced by

$$g = C + A \exp \left[ - \left( \left[ \frac{i'}{\sigma} \right]^2 + \left[ \frac{j'a}{\sigma} \right]^2 \right)^b \right]. \tag{A4}$$

### Appendix E. Basic Data Structure

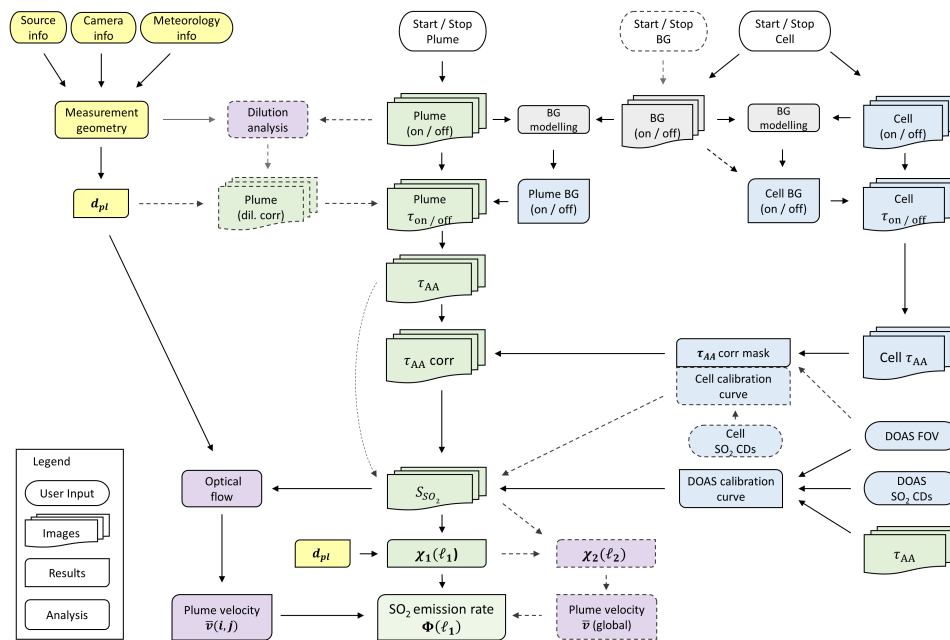


**Figure A1.** Main analysis steps. Flowchart showing the main analysis steps for emission rate retrievals (cf. Table 1). The colours indicate geometrical calculations (yellow), background modelling (light gray), camera calibration (light blue), plume velocity retrieval (light purple) and the central processing steps for the emission rate retrieval (light green). Shaded and dashed symbols indicate optional or alternative analysis methods. Note that the colour scheme is not related to the scheme used in Figure 2.

The *Pyplis* code hierarchy for the emission rate analysis is shown in Figure 2. The structure is based on the work flow shown in Figure A1 and includes most of the relevant classes required for the emission rate analysis.

#### Appendix E.1. Setup and Dataset Classes

The most important classes related to data import and image management are:

- Setup classes (e.g., *Camera*, *Source*, *MeasSetup*), which can be used to specify all relevant meta information.
- Dataset classes (*Dataset*, *CellCalibEngine*), which can be used for automatic image separation, for instance by image type (e.g., on, off, dark, offset) or acquisition time.

#### Appendix E.2. ImgList classes

Image list classes are central for the data analysis. They can be found in the *imagelists.py* module (e.g., *ImgLisxt*, *CellImgList*). An *ImgList* typically contains images of one specific type (e.g., on-band) corresponding to a certain time window. In order to avoid potential memory overflows, images are loaded, processed and unloaded successively within *ImgList* objects. The most important features are described in the following.

##### Appendix E.2.1. Linking of *ImgList* Objects

*ImgList* can be linked to each other (e.g., off to on-band list). This means that, whenever the list index (i.e., the current image) is changed in *ImgList A* (e.g., the on-band images), it is also changed in *ImgList B* (if *B* is linked to *A*), such that the current image in *B* is closest in time to the one in *A*.

## Appendix E.2.2. Image Preparation and Processing Modes

Image lists include several image preparation options (e.g., size reduction, cropping, blurring). Furthermore, if certain requirements are fulfilled, additional preparation options and routines can be activated:

- ***darkcorr\_mode*** → images are automatically corrected for dark and offset and requires a dark image (or an `ImgList` containing dark images) to be available in the list. For dark correction mode 1 (see appendix C), an offset image (or list) must also be available.
- ***tau\_mode*** → if active, images are converted into  $\tau$  images on image load (using the `PlumeBackgroundModel` class to retrieve the plume background intensities) and requires availability of a sky reference image in the list (only for background modelling methods 1–6, see Section 3.3).
- ***aa\_mode*** → if active, images are converted into  $\tau_{AA}$  images on image load and requires an off-band image list to be linked to the list and availability of a sky reference image in both lists (only for background modelling methods 1–6, see Section 3.3).
- ***dilcorr\_mode*** → if active, images are loaded as dilution corrected images (cf. Section 3.6) and requires extinction coefficients to be available in the list (list attribute `ext_coeffs`, cf. example script 11). Furthermore, availability of plume distances (list attribute `plume_dists`) and pre-computation of a  $\tau$ -image (see two points above) is required to retrieve a boolean mask specifying plume-pixels (identified from the  $\tau$ -image using a provided  $\tau$  threshold).
- ***sensitivity\_corr\_mode*** → if active, images will be corrected for sensitivity variations due to shifts in the filter transmission windows (see Section 2.2) and requires a corresponding correction mask to be available in the list. The latter can, for instance, be retrieved from cell calibration data (see Section 3.4.1).
- ***calib\_mode*** → if active, images are loaded as calibrated SO<sub>2</sub>-CD images and requires the list to be in *aa\_mode* and calibration data to be available in the list. The latter can be of type `CellCalibData` or `DoasCalibData` (see Figure 2), and warns if *sensitivity\_corr\_mode* is inactive.
- ***optflow\_mode*** → if active, the Farnebäck optical flow will be calculated between current and the next list image (using the `OptflowFarneback` class, see Section 3.5.2).
- ***vigncorr\_mode*** → if active, images will be corrected for vignetting and requires availability of a vignetting mask in the list or a sky reference image from which the mask is determined.

All active image preparation options are applied on image load (i.e., whenever the current image is changed in the `ImgList`).

## Appendix E.3. Processing Classes

Most of the relevant processing classes are shown in Figure 2. They include:

- `MeasGeometry` (*geometry.py*) → all relevant geometrical calculations (Section 3.1).
- `OptflowFarneback` (*plumespeed.py*) → calculation and post analysis of optical flow field between two images (Section 3.5.2).
- `CellCalibData` (*cellcalib.py*) → pixel based retrieval of cell calibration polynomial (based on a set of cell  $\tau$  images) and retrieval of sensitivity correction mask (Section 3.4.1).
- `DoasFovEngine` (*doascalib.py*) → performs FOV search of DOAS spectrometer within camera images (Section 3.4.2 and Appendix D).
- `DoasFov` (*doascalib.py*) → DOAS FOV information such as position, shape, convolution mask (Section 3.4.2 and Appendix D), can be saved as FITS file.
- `DoasCalibData` (*doascalib.py*) → DOAS calibration data, i.e., vector of  $\tau$  and SO<sub>2</sub>-CD values for fitting of calibration polynomial (Section 3.4.2), can be saved as FITS file.
- `LineOnImage` (*processing.py*) → data extraction (interpolation) along a line on a discrete 2D image grid (e.g., SO<sub>2</sub>-CDs from calibrated images or displacement vectors from optical flow field, Section 3.7).

- `EmissionRateAnalysis` (`fluxcalc.py`) → Performs emission rate analysis based on an `ImgList` containing calibrated images. Emission rates can be retrieved along one (or more) plume cross section lines (`LineOnImage` objects) and has several options related to the plume velocity retrieval (Section 3.7).
- `EmissionRates` (`fluxcalc.py`) → Contains results (time series) of an emission rate analysis (i.e., including plume velocity data), specific for one PCS line and one velocity retrieval (e.g., the analysis shown in Figure 11 creates three `EmissionRates` objects for each of the three different velocity retrievals, Section 3.7).

Further important classes (not shown in Figure 2) are:

- `PlumeBackgroundModel` (`plumebackground.py`) → performs  $\tau$  image modelling using either of the available modelling methods (Section 3.3).
- `VeloCrossCorrEngine` (`plumespeed.py`) → high level class to calculate the plume velocity using the cross-correlation method (Section 3.5.1).
- `DilutionCorr` (`dilutioncorr.py`) → engine to perform signal dilution correction (Section 3.6).
- `ImgStack` (`processing.py`) → contains a series of images (stored as 3D numpy array) as well as supplementary data (e.g., acq. time stamps, exposure times of all stacked images) and basic processing operations (time merging with other data, up / downscaling), can be saved as FITS file.

## Appendix F. Supplementary Information and Test Data

### Appendix F.1. Example Dataset and Example Scripts

Most of the example and introduction scripts provided with *Pyplis* are based on a short example dataset recorded at Mt. Etna, Italy on 16 September 2015, using a type Envicam-2 camera. It includes ~15 min of plume data (between 7:06 a.m. and 7:22 a.m. UTC, see e.g., Figure 11.) as well as cell calibration data including suitable background images (between 6:59 a.m. and 7:04 a.m. UTC, see Figure 5). These data are used for demonstration purposes in the provided example scripts, which are summarised in Table A2. The data is not part of the *Pyplis* installation and can be downloaded from the website.

**Table A2.** *Pyplis* example scripts, sub-categorised into introductory scripts (0.1–0.7) and scripts related to the emission rate analysis of the Etna test data (1–12).

No.	Name	Description	Section
0.1	ex0_1_img_handling.py	The <code>Img</code> class - Image import and dark correction	3.2
0.2	ex0_2_camera_setup.py	The <code>Camera</code> class - Definition of camera specifications and image file name convention	E
0.3	ex0_3_imglists_manually.py	Introduction into <code>ImgList</code> objects	E.2
0.4	ex0_4_imglists_auto.py	Automatic creation of <code>ImgList</code> objects using the ECII default <code>Camera</code> type	E.2
0.5	ex0_5_optflow_livecam.py	Interactive optical flow using web cam	3.5.2
0.6	ex0_6_pcs_lines.py	Plume cross section lines (creation and orientation of <code>LineOnImage</code> objects)	3.7
0.7	ex0_7_cellcalib_manual.py	Introduction into cell calibration and the <code>CellCalibData</code> object (manually)	3.4.1
1	ex01_analysis_setup.py	Create <code>MeasSetup</code> class and initiate analysis <code>Dataset</code> object from that (see Figure 2)	3.4.1
2	ex02_meas_geometry.py	Introduction into the <code>MeasGeometry</code> class	3.1
3	ex03_plume_background.py	The <code>PlumeBackgroundModel</code> class - background modelling and $\tau$ image retrieval	3.3
4	ex04_prep_aa_imglist.py	Preparation of image list containing AA images	E.2
5	ex05_cell_calib_auto.py	Automatic cell calibration using the <code>CellCalibEngine</code> class	3.4.1
6	ex06_doas_calib.py	DOAS calibration and FOV search	3.4.2
7	ex07_doas_cell_calib.py	Retrieval of AA sensitivity correction mask	3.4
8	ex08_velo_crosscorr.py	Plume velocity retrieval using cross-correlation	3.5.1
9	ex09_velo_optflow.py	Plume velocity retrieval using Farnebäck optical flow algorithm using <code>OptflowFarneback</code> class	3.5.2
10	ex10_bg_imglists.py	Retrieval of background image lists (on, off) using <code>Dataset</code> class	E
11	ex11_signal_dilution.py	Correction for signal dilution and the <code>DilutionCorr</code> class	3.6
12	ex12_emission_rate.py	Emission rate retrieval for the test dataset	3.7
	SETTINGS.py	Global settings for example scripts	

### Appendix F.2. Camera Specifications

In order to use all features of *Pyplis* (e.g., automatic file separation, automatic dark and offset correction, geometrical calculations), certain camera characteristics need to be provided by the user. This information is typically specified within a *Camera* class (*setupclasses.py* module). The required information includes specifications about the image sensor (e.g., pixel geometry) and optics (e.g., focal length) as well as file naming conventions (e.g., how to retrieve the filter type or the image acquisition time from file names). *Pyplis* provides the possibility to define new default camera types that store all relevant camera information to the *Pyplis* data file *cam\_info.txt*, which can be found in the *data* directory of the installation (see example script 0.2 for details).

### Appendix F.3. Source Specifications

Default source information (e.g., longitude, latitude, altitude) can be specified in the file *my\_sources.txt* in the installation *data* directory.

## References

1. Robock, A. Volcanic eruptions and climate. *Rev. Geophys.* **2000**, *38*, 191–219.
2. IPCC. *Climate Change 2013: The Physical Science Basis. Contribution of Working Group I to the Fifth Assessment Report of the Intergovernmental Panel on Climate Change*; Cambridge University Press: Cambridge, UK, 2013; p. 1535.
3. Carroll, M.R.; Holloway, J.R. *Volatiles in Magmas*; Mineralogical Society of America: Chantilly, VA, USA, 1994.
4. Oppenheimer, C.; Fischer, T.; Scaillet, B. 4.4 - Volcanic Degassing: Process and Impact. In *Treatise on Geochemistry, 2nd ed.*; Elsevier: Amsterdam, The Netherlands, 2014; pp. 111–179.
5. Lübcke, P.; Bobrowski, N.; Arellano, S.; Galle, B.; Garzón, G.; Vogel, L.; Platt, U. BrO / SO<sub>2</sub> molar ratios from scanning DOAS measurements in the NOVAC network. *Solid Earth* **2014**, *5*, 409–424.
6. Bobrowski, N.; von Glasow, R.; Giuffrida, G.B.; Tedesco, D.; Aiuppa, A.; Yalire, M.; Arellano, S.; Johansson, M.; Galle, B. Gas emission strength and evolution of the molar ratio of BrO/SO<sub>2</sub> in the plume of Nyiragongo in comparison to Etna. *J. Geophys. Res. Atmos.* **2015**, *120*, 277–291.
7. Moffat, A.J.; Millan, M.M. The applications of optical correlation techniques to the remote sensing of SO<sub>2</sub> plumes using sky light. *Atmos. Environ. (1967)* **1971**, *5*, 677–690.
8. Platt, U.; Stutz, J. *Differential Optical Absorption Spectroscopy: Principles and Application*; Springer: New York, NY, USA, 2008.
9. Platt, U.; Perner, D. Direct measurements of atmospheric CH<sub>2</sub>O, HNO<sub>2</sub>, O<sub>3</sub>, NO<sub>2</sub>, and SO<sub>2</sub> by differential optical absorption in the near UV. *J. Geophys. Res.* **1980**, *85*, 7453–7458.
10. Galle, B.; Johansson, M.; Rivera, C.; Zhang, Y.; Kihlman, M.; Kern, C.; Lehmann, T.; Platt, U.; Arellano, S.; Hidalgo, S. Network for Observation of Volcanic and Atmospheric Change (NOVAC)—A global network for volcanic gas monitoring: Network layout and instrument description. *J. Geophys. Res.* **2010**, *115*, doi:10.1029/2009JD011823.
11. Mori, T.; Burton, M. The SO<sub>2</sub> camera: A simple, fast and cheap method for ground-based imaging of SO<sub>2</sub> in volcanic plumes. *Geophys. Res. Lett.* **2006**, *33*, doi:10.1029/2006GL027916.
12. Bluth, G.; Shannon, J.; Watson, I.; Prata, A.; Realmuto, V. Development of an ultra-violet digital camera for volcanic SO<sub>2</sub> imaging. *J. Volcanol. Geotherm. Res.* **2007**, *161*, 47–56.
13. Kantzas, E.P.; McGonigle, A.J.S.; Tamburello, G.; Aiuppa, A.; Bryant, R.G. Protocols for UV camera volcanic SO<sub>2</sub> measurements. *J. Volcanol. Geotherm. Res.* **2010**, *194*, 55–60.
14. Stebel, K.; Amigo, A.; Thomas, H.; Prata, A. First estimates of fumarolic SO<sub>2</sub> fluxes from Putana volcano, Chile, using an ultraviolet imaging camera. *J. Volcanol. Geotherm. Res.* **2015**, *300*, 112–120.
15. McGonigle, A.J.S.; Pering, T.D.; Wilkes, T.C.; Tamburello, G.; D’Aleo, R.; Bitetto, M.; Aiuppa, A.; Willmott, J.R. Ultraviolet Imaging of Volcanic Plumes: A New Paradigm in Volcanology. *Geosciences* **2017**, *7*, 68.
16. D’Aleo, R.; Bitetto, M.; Delle Donne, D.; Tamburello, G.; Battaglia, A.; Coltelli, M.; Patanè, D.; Prestifilippo, M.; Scotto, M.; Aiuppa, A. Spatially resolved SO<sub>2</sub> flux emissions from Mt Etna. *Geophys. Res. Lett.* **2016**, *43*, 7511–7519.

17. Sweeney, D.; Kyle, P.R.; Oppenheimer, C. Sulfur dioxide emissions and degassing behavior of Erebus volcano, Antarctica. *J. Volcanol. Geotherm. Res.* **2008**, *177*, 725–733.
18. Nicholson, E.; Mather, T.; Pyle, D.; Odbert, H.; Christopher, T. Cyclical patterns in volcanic degassing revealed by SO<sub>2</sub> flux timeseries analysis: An application to Soufrière Hills Volcano, Montserrat. *Earth Planet. Sci. Lett.* **2013**, *375*, 209–221.
19. Tamburello, G.; Aiuppa, A.; McGonigle, A.J.S.; Allard, P.; Cannata, A.; Giudice, G.; Kantzas, E.P.; Pering, T.D. Periodic volcanic degassing behavior: The Mount Etna example. *Geophys. Res. Lett.* **2013**, *40*, 4818–4822.
20. Kern, C.; Kick, F.; Lübcke, P.; Vogel, L.; Wöhrbach, M.; Platt, U. Theoretical description of functionality, applications, and limitations of SO<sub>2</sub> cameras for the remote sensing of volcanic plumes. *Atmos. Meas. Tech.* **2010**, *3*, 733–749.
21. Lübcke, P.; Bobrowski, N.; Illing, S.; Kern, C.; Alvarez Nieves, J.M.; Vogel, L.; Zielcke, J.; Delgado Granados, H.; Platt, U. On the absolute calibration of SO<sub>2</sub> cameras. *Atmos. Meas. Tech.* **2013**, *6*, 677–696.
22. Champion, R.; Delgado-Granados, H.; Mori, T. Image-based correction of the light dilution effect for SO<sub>2</sub> camera measurements. *J. Volcanol. Geotherm. Res.* **2015**, *300*, 48–57.
23. Peters, N.; Hoffmann, A.; Barnie, T.; Herzog, M.; Oppenheimer, C. Use of motion estimation algorithms for improved flux measurements using SO<sub>2</sub> cameras. *J. Volcanol. Geotherm. Res.* **2015**, *300*, 58–69.
24. Kern, C.; Lübcke, P.; Bobrowski, N.; Champion, R.; Mori, T.; Smekens, J.F.; Stebel, K.; Tamburello, G.; Burton, M.; Platt, U.; et al. Intercomparison of SO<sub>2</sub> camera systems for imaging volcanic gas plumes. *J. Volcanol. Geotherm. Res.* **2015**, *300*, 22–36.
25. Tamburello, G.; Kantzas, E.; McGonigle, A.J.S.; Aiuppa, A. Vulcamera: A program for measuring volcanic SO<sub>2</sub> using UV cameras. *Ann. Geophys.* **2011**, *54*, 219–221.
26. Peters, N. Plumetrack SO<sub>2</sub> Flux Calculator. 2014. Available online: <https://ccpforge.cse.rl.ac.uk/gf/project/plumetrack/> (accessed on 11 September 2017).
27. Gliß, J.; Stebel, K.; Kylling, A.; Dinger, A.S.; Sihler, H.; Sudbø, A. Pyplis Website. 2017. GitHub. Available online: <https://github.com/jgliss/pyplis> (accessed on 13 December 2017).
28. Gliß, J.; Stebel, K.; Kylling, A.; Dinger, A.S.; Sihler, H.; Sudbø, A. Pyplis Website. 2017. Documentation Website. Available online: <https://pyplis.readthedocs.io> (accessed on 13 December 2017).
29. Kern, C.; Sutton, J.; Elias, T.; Lee, L.; Kamibayashi, K.; Antolik, L.; Werner, C. An automated SO<sub>2</sub> camera system for continuous, real-time monitoring of gas emissions from Kilauea Volcano's summit Overlook Crater. *J. Volcanol. Geotherm. Res.* **2015**, *300*, 81–94.
30. Sihler, H.; Lübcke, P.; Lang, R.; Beirle, S.; de Graaf, M.; Hörmann, C.; Lampel, J.; Penning de Vries, M.; Remmers, J.; Trollope, E.; et al. In-operation field-of-view retrieval (IFR) for satellite and ground-based DOAS-type instruments applying coincident high-resolution imager data. *Atmos. Meas. Tech.* **2017**, *10*, 881–903.
31. Kern, C.; Werner, C.; Elias, T.; Sutton, A.J.; Lübcke, P. Applying UV cameras for SO<sub>2</sub> detection to distant or optically thick volcanic plumes. *J. Volcanol. Geotherm. Res.* **2013**, *262*, 80–89.
32. McGonigle, A.J.S.; Hilton, D.R.; Fischer, T.P.; Oppenheimer, C. Plume velocity determination for volcanic SO<sub>2</sub> flux measurements. *Geophys. Res. Lett.* **2005**, *32*, L11302.
33. Klein, A.; Lübcke, P.; Bobrowski, N.; Kuhn, J.; Platt, U. Plume propagation direction determination with SO<sub>2</sub> cameras. *Atmos. Meas. Tech.* **2017**, *10*, 979–987.
34. Kern, C.; Deutschmann, T.; Vogel, L.; Wöhrbach, M.; Wagner, T.; Platt, U. Radiative transfer corrections for accurate spectroscopic measurements of volcanic gas emissions. *Bull. Volcanol.* **2010**, *72*, 233–247.
35. Kern, C.; Deutschmann, T.; Werner, C.; Sutton, A.J.; Elias, T.; Kelly, P.J. Improving the accuracy of SO<sub>2</sub> column densities and emission rates obtained from upward-looking UV-spectroscopic measurements of volcanic plumes by taking realistic radiative transfer into account. *J. Geophys. Res. Atmos.* **2012**, *117*, doi:10.1029/2012JD017936.
36. Vogel, L.; Galle, B.; Kern, C.; Delgado Granados, H.; Conde, V.; Norman, P.; Arellano, S.; Landgren, O.; Lübcke, P.; Alvarez Nieves, J.M.; et al. Early in-flight detection of SO<sub>2</sub> via Differential Optical Absorption Spectroscopy: A feasible aviation safety measure to prevent potential encounters with volcanic plumes. *Atmos. Meas. Tech.* **2011**, *4*, 1785–1804.
37. Gliß, J. Geonum. 2016. Available online: <https://github.com/jgliss/geonum> (accessed on 11 September 2017).

38. Farr, T.G.; Rosen, P.A.; Caro, E.; Crippen, R.; Duren, R.; Hensley, S.; Kobrick, M.; Paller, M.; Rodriguez, E.; Roth, L.; et al. The Shuttle Radar Topography Mission. *Rev. Geophys.* **2007**, *45*, doi:10.1029/2005RG000183.
39. Amante, C.; Eakins, B.W. ETOPO1 Global Relief Model converted to PanMap layer format. *NOAA-Natl. Geophys. Data Center PANGAEA* **2009**, doi:10.1594/PANGAEA.769615.
40. Kraus, S. DOASIS: A framework design for DOAS. Ph.D. Thesis, Universitat Mannheim, Mannheim, Germany, 2006.
41. Farneböck, G., Two-Frame Motion Estimation Based on Polynomial Expansion. In Proceedings of the 13th Scandinavian Conference on Image Analysis, (SCIA 2003), Halmstad, Sweden, 29 June–2 July 2003; Springer: Berlin, Germany, 2003; pp. 363–370.
42. Bradski, G. The OpenCV Library. *Dr. Dobb's J. Softw. Tools* **2000**, *25*, 120–123.
43. Gliß, J.; Stebel, K.; Kylling, A.; Sudbø, A. Optical flow gas velocity analysis in plumes using UV cameras—Implications for SO<sub>2</sub>-emission rate retrievals investigated at Mt. Etna, Italy, and Guallatiri, Chile. *Atmos. Meas. Tech. Discuss.* **2017**, *2017*, 1–30.
44. Fong, D.C.L.; Saunders, M. LSMR: An Iterative Algorithm for Sparse Least-Squares Problems. *SIAM J. Sci. Comput.* **2011**, *33*, 2950–2971.

**Sample Availability:** The *Pyplis* software is freely available, including the example data and scripts. For more information see <http://pyplis.readthedocs.io>.



© 2017 by the authors. Licensee MDPI, Basel, Switzerland. This article is an open access article distributed under the terms and conditions of the Creative Commons Attribution (CC BY) license (<http://creativecommons.org/licenses/by/4.0/>).